

## Symposium-in-Print

# Regional Imager for Low-Resolution Functional Imaging of the Brain with Diffusing Near-Infrared Light

R. M. Danen<sup>\*1,2</sup>, Yong Wang<sup>1</sup>, X. D. Li<sup>2</sup>, W. S. Thayer<sup>1</sup> and A. G. Yodh<sup>\*2</sup>

<sup>1</sup>NIM Incorporated, Philadelphia, PA, USA and

<sup>2</sup>Department of Physics and Astronomy, University of Pennsylvania, Philadelphia, PA, USA

Received 17 June 1997; accepted 16 October 1997

### ABSTRACT

We have developed a near-infrared spectroscopy system for low-resolution regional imaging of the brain. Our regional imager employs two intensity-modulated (frequency-domain) diode lasers operating at 779 and 834 nm, respectively, in order to produce macroscopic waves of diffusing photons. The interaction of these diffusive waves with tissue depends on laser modulation frequency, laser wavelength and the optical properties of the sample tissue volume. The lasers can be modulated over a range of frequencies from 50 to 400 MHz. Light is coupled to and from the head using a pad that has 12 source and 4 detector positions within an area of approximately 40 cm<sup>2</sup>. The pad can be moved to different positions on the head. Measurements from different source–detector combinations enable reconstruction of low-resolution images of the tissue volume beneath the pad. For example, we have made two-dimensional back-projection images of model systems in order to demonstrate the capabilities of the regional imager. We also present preliminary results from initial clinical studies at the Children's Hospital of Philadelphia.

### 1. INTRODUCTION AND BACKGROUND

The application of diffusing near-infrared light for the study of tissue structure and metabolism has been the subject of intense recent interest (1,2). In particular, diffuse photon density waves (3–9) and their time-domain analogs (10–13) have been used to provide quantitative spectroscopic information about chromophores such as oxyhemoglobin (OxyHb)† and deoxyhemoglobin (DeoxyHb) in a variety of tissues, including brain tissue. Furthermore, the possibility of projection and tomographic imaging with these waves has

been explored experimentally with success in tissue phantoms (14–20) and *in vivo* (21–23). While the spatial resolution of the optical method is limited to ~1 cm<sup>3</sup> (24), the mechanisms of contrast, the tissue penetration, the speed and the cost of these new techniques offer the possibility for diagnostic improvements over conventional radiologic instruments.

In this contribution we describe a near-infrared instrument, the regional imager, that we have developed for the purposes of low-resolution functional imaging of the brain (particularly the baby brain). Near-infrared light can penetrate centimeters into the scalp, skull, dura and brain, making possible a range of investigations. For example, near-infrared spectroscopy has been used to detect cerebral hypoxia and changes in cerebral blood volume (25–28). We anticipate that the regional imager will enable the evaluation of critical care conditions such as hydrocephalus and hematoma, as well as providing a method to probe blood oxygenation during heart surgery and cognition studies. In general, the instrument is capable of providing rapid, projection images of the tissue volume below the device surface. Thus the regional imager may be valuable in environments such as neurology clinics, emergency rooms, operating rooms and intensive care units, where there are few economical or convenient methods currently available to diagnose intracranial disease.

To these ends, the regional imager was designed to be fast and easy to use. Furthermore, rather than develop a comprehensive optical imaging instrument for the whole brain, we instead developed an intermediate device that is faster and more directed than a “complete” brain imager (13,14) and improves upon purely spectroscopic near-infrared probes (29–35) wherein the sample medium is assumed to be homogeneous. The new device offers the possibility for reconstruction of optical properties with linear resolutions of ~1 cm. The instrument consists of multiple source and detector positions located on a 4 cm × 9 cm rectangular area called the optical pad (see Fig. 1). Measurements from different source and detector positions on the optical pad probe different regions of tissue; this provides information sufficient for reconstruction of an image. The regional imager uses two wavelengths (779 and 834 nm) to determine the oxygenation level of blood.

\*To whom correspondence should be addressed at: Dept. of Physics and Astronomy, University of Pennsylvania, Philadelphia, PA 19104, USA. Fax: 215-898-2010.

†Abbreviations: APD, avalanche photodiode; DeoxyHb, deoxyhemoglobin; OxyHb, oxyhemoglobin; RF, radio frequency; SSB, single-sideband mixer.

© 1998 American Society for Photobiology 0031-8655/98 \$5.00+0.00

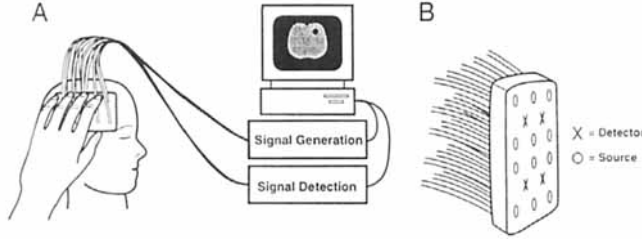


**Figure 1.** Schematic of the regional imager (A) and the source-detector geometry of the optical pad (B). The pad is semiflexible and can conform to the curves of the head.

The following section provides basic theoretical background about diffuse photon density waves. Then, section 3 describes the instrument and section 4 describes the back-projection approach we have been using for rapid reconstruction of images. Finally, sections 5 and 6 present experimental results that illustrate the potential performance of the regional imager.

## 2. DIFFUSE PHOTON DENSITY WAVES

The operation of the regional imager is based on the use of diffuse photon density waves. Diffuse photon density waves are scalar, overdamped traveling waves of photon density (3–9). They will propagate through turbid media such as tissue (for near-infrared light) wherein the transport of light energy density,  $U(\vec{r}, t)$ , is governed by a diffusion equation. A light source, with an intensity modulated at frequency  $\omega$ , generates a diffuse photon density wave in an optically turbid medium. For a sinusoidally modulated source, the resultant diffusive wave obeys a Helmholtz equation; it therefore exhibits many properties that we normally associate with conventional electromagnetic waves such as refraction (4), diffraction (5,6), dispersion (7,8), interference (9) and scattering (5).

The simplest model for the experiments we perform treats the sample as a semi-infinite medium. In this case, each source and detector on the pad are separated by a distance  $\rho$  along the surface of the sample as shown in Fig. 2. The incident light field (laser light delivered by optical fiber) is approximated as a point source displaced a distance  $z_{tr} = 1/\mu'_s$  (1 mean free path) into the medium, where  $\mu'_s$  is the reduced scattering coefficient of the medium. The spatial part of the time-dependent component of the energy density of the diffusive wave at position  $\vec{r}$  in the sample can be described by the following simple solution for this geometry:

$$U(\vec{r}) = \frac{S}{4\pi D} \left[ \frac{\exp(ik|\vec{r} - \vec{r}_s|)}{|\vec{r} - \vec{r}_s|} - \frac{\exp(ik|\vec{r} - \vec{r}_I|)}{|\vec{r} - \vec{r}_I|} \right] \quad (1)$$

where  $\vec{r}_s$  is the position of the point source,  $\vec{r}_I$  is the position of the image source (using extrapolated boundary conditions) located as shown in Fig. 2, and  $S$  represents the initial amplitude and phase of the source. The wavenumber  $k$  and the light diffusion coefficient  $D$  are given by

$$k^2 = \frac{-\nu\mu_a + i\omega}{D} \quad \text{and} \quad D = \frac{\nu}{3\mu'_s} \quad (2)$$

where  $\nu$  is the speed of light in the diffusive medium and  $\mu_a$  is the absorption coefficient of the medium. When the source-detector separations are larger than the transport

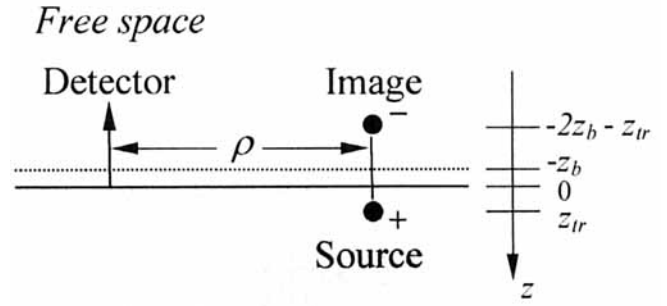


**Figure 2.** The semi-infinite medium model showing source, detector, their separation  $\rho$  and image source. The dashed line shows the extrapolated zero boundary.

mean free path (i.e.  $\rho \gg z_{tr}$ , where  $z_{tr} \sim 1$  mm for tissues), then Eq. 1 simplifies to the following form,

$$U(\rho) = \frac{S}{4\pi D} \frac{\exp(ik\rho)}{\rho^2} [-2ik(z_b^2 + z_b z_{tr})], \quad \text{where} \quad (3)$$

$$z_b = \frac{2}{3\mu'_s}.$$

We do not use a reflection coefficient to determine the extrapolated boundary  $z_b$  (36), because the optical pad (black piece of rubber or foam) touches the edge of the sample. In any case, inclusion of a reflection coefficient resulting from a mismatch in refractive indices at the sample-pad interface does not significantly affect our results.

The absorption and scattering coefficients of the medium can be determined directly from measurements of the amplitude and phase of the diffusive wave. Letting  $k = k_r + ik_i$ , where  $k_r$  and  $k_i$  are the real and imaginary parts of  $k$ , respectively, we can express the absorption coefficient  $\mu_a$  and the scattering coefficient  $\mu'_s$  as

$$\mu_a = \frac{\omega}{\nu} \left[ \tan \left( 2 \tan^{-1} \frac{k_r}{k_i} \right) \right]^{-1} \quad \text{and} \quad \mu'_s = \frac{k_r^2 + k_i^2}{3\sqrt{\mu_a'^2 + (\omega/\nu)^2}}. \quad (4)$$

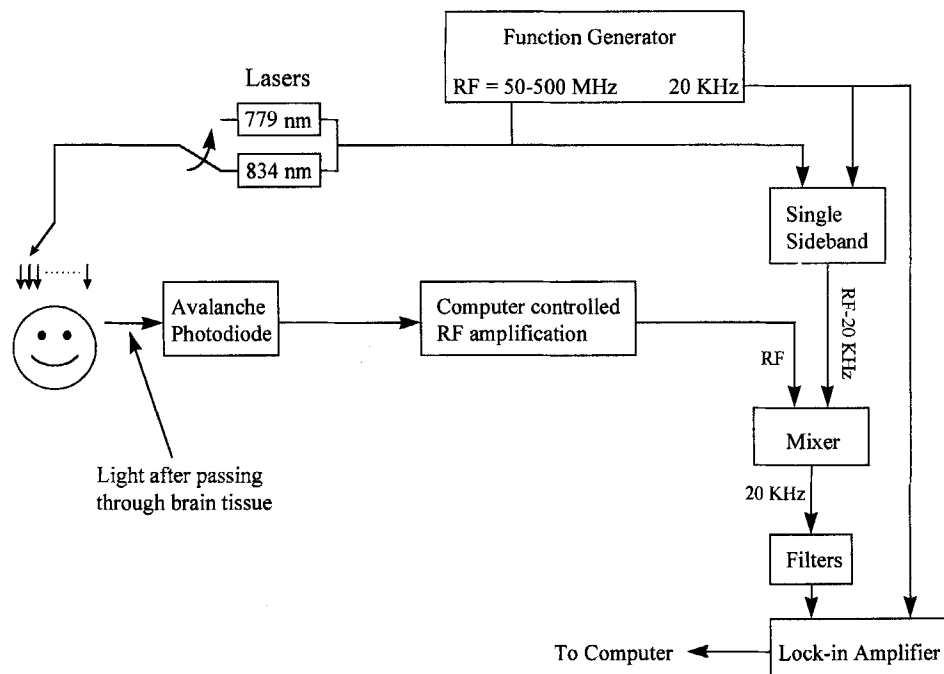
We determine the real and imaginary parts of  $k$  from the measured  $U(\rho)$  to determine  $\mu_a$  and  $\mu'_s$ .

Images may be obtained in a variety of ways; for example, as discussed below, we may associate a weight with each volume element (or voxel) in the sample that depends on the location of the source and detector of each source-detector pair relative to the location of the voxel.

## 3. INSTRUMENT DESIGN

The regional imager (see Fig. 1) is a near-infrared imaging instrument composed of multiple source and detector positions. Light is sent to and from the head *via* optical fibers; the optical pad, shown in Fig. 1B, positions the fibers against the head. The pad is a semiflexible, sturdy rubber sheet that holds 12 source fibers and 4 detector fiber bundles, arranged in a 9 cm  $\times$  4 cm rectangular area. This gives separations (on a flat surface) between sources and detectors ranging from 2 to 8 cm. The flexibility of the pad allows placement of the fibers against the curved head. The optical pad can

**Figure 3.** Electronic configuration of the regional imager. The regional imager contains four identical detection circuits that include an avalanche photodiode, computer-controlled attenuator/amplifier electronics, mixer filters and lock-in amplifier.



be moved to different positions on the head. Two fiber multiplexers are employed (see Fig. 3); the first multiplexer selects one of the two laser sources for the second fiber multiplexer, which in turn sequentially couples the selected source to 1 of the 12 source positions on the pad. The laser power leaving the pad is  $\sim 10$  mW, and the source fibers are 140  $\mu\text{m}$  in diameter. The four detector bundles (6 mm diameter multimode fiber bundles) on the pad couple the diffusive waves, after they travel through the head, into four parallel electronic detection channels. A complete measurement at a single wavelength and single modulation frequency takes 2.5 minutes.

Figure 3 shows the electronic configuration of the regional imager. The intensity of each laser is modulated at a radio frequency (RF) by voltage signals from an RF function generator. The system can operate at selectable frequencies ranging from 50 to over 400 MHz in order to produce diffuse photon density waves in the sample oscillating with the selected modulation frequency. In principle, measurements using several modulation frequencies should enable better separation of tissue scattering from tissue absorption. The function generator also provides a low-frequency reference signal (20 kHz) that is separately coupled into a single-sideband mixer (SSB) along with the modulation signal. The output from the SSB is an RF signal with a frequency shift of 20 kHz from the source modulation frequency. This signal is mixed with the amplified RF output from the avalanche photodiode (APD) light detectors that measure the transmitted diffusive waves. The low-frequency (20 kHz) component of the mixed output passes through filters and is measured with a lock-in amplifier. The lock-in amplifiers thus determine the amplitude and the phase of the transmitted diffusive wave. A personal computer is used to read and record data from the lock-in amplifiers, as well as to adjust the amplification, by means of a programmable step attenuator, of the signal leaving the APDs so that, whenever possible, it is within the

optimal range of the mixer and lock-in amplifier. The dynamic range of the instrument is  $\sim 10^4$ . The computer is also used for rapid calculation of the average optical properties of the tissue volume under the pad and for image reconstruction.

#### 4. IMAGE RECONSTRUCTION ALGORITHM

Many methods have been developed to reconstruct images of the sample volume from measurements of amplitude and phase of the diffusive wave (14–23). For the present study, we chose a simple method because it is computationally fast. In particular, we employ a back-projection approach with a voxel weighting factor that is essentially the three-point-Green's function of the medium underlying the pad using the average optical properties of the medium (37). This approach has the advantage that it is very fast and conceptually simple and thus offers a quick two-dimensional image of the underlying tissue volume. It has the disadvantage in that it is an empirical approach and is not as accurate as the perturbation methods. Thus, it is useful for detecting trends but does not accurately reconstruct the optical properties of inhomogeneities. Because we record all data from the measurements, we will be able to explore the utility of other computationally intensive algorithms for situations where speed is not essential.

In our back-projection approach, we first combine measurements from all source–detector pairs to derive the average absorption and scattering coefficients of the entire medium underlying the optical pad. These average values of absorption and scattering are then used in all of the weight functions employed in the reconstructions.

If the medium is truly homogeneous and semi-infinite, then the absorption and scattering coefficients of the medium can be determined directly from measurements of the amplitude and phase of the diffusive wave using, for example,

a set of source–detector pairs with differing separations  $\rho$ . The real and imaginary parts of  $k$  are found from the slopes of the lines describing the amplitude (more precisely, the natural logarithm of  $\rho^2|U(\rho)|$ ) and phase ( $\phi = \tan^{-1}[\text{Im}\{U\}/\text{Re}\{U\}]$ ) of the diffusive wave measured for each source–detector pair ( $sd$ ) as a function of their separation distance  $\rho$  (1). This follows from the form of the solution in Eq. 3, which can be rewritten as

Amplitude:

$$\ln(\rho^2|U(\rho)|) = -k_i\rho + \ln\left(\frac{|S|}{2\pi D}[z_b^2 + z_b z_{tr}]\sqrt{k_r^2 + k_i^2}\right) \quad (5)$$

Phase:

$$\phi(\rho) = k_r\rho - \tan^{-1}(k_r/k_i) + \phi_{\text{source}}. \quad (6)$$

Here  $\phi_{\text{source}}$  is the initial phase of the source. The slopes of these lines give the imaginary and real parts of  $k$ . We have assumed that the media are reasonably well approximated as semi-infinite, and that we can employ Eqs. 5 and 6 to obtain an immediate estimate of the average absorption and scattering coefficients of the underlying medium.

The next step is to determine the absorption and scattering coefficients for each source–detector pair. This is accomplished by numerically solving Eqs. 5 and 6, using the measurements from the source–detector pair, for the real and imaginary parts of  $k$ , and then using Eq. 4 to determine the absorption and scattering coefficients. These values will be denoted as  $\mu_a^M(\rho_{sd})$  and  $\mu_s^M(\rho_{sd})$ , where the superscript  $M$  denotes the Measured value of the absorption or scattering coefficient as determined by the particular source–detector pair  $sd$ . The parameters  $D$ ,  $z_{tr}$  and  $z_b$  in Eq. 5 are determined by the average scattering coefficient of the medium.

Once  $\mu_a^M(\rho_{sd})$  and  $\mu_s^M(\rho_{sd})$  are determined for each source–detector pair, the values  $\mu_a^M(\rho_{sd})$  and  $\mu_s^M(\rho_{sd})$  are combined in a weighting scheme in order to determine  $\mu_a$  and  $\mu_s$  in a planar slice of the turbid medium that is parallel to the optical pad. Specifically, the planar slice is divided into voxels (see Fig. 4). For each voxel, measurements from the different source–detector pairs are combined using weights that depend on the distance between the source and the voxel ( $r_{sv}$ ), the distance between the voxel and the detector ( $r_{vd}$ ) and the complex wavenumber ( $k$ ) as defined using the average optical properties of the medium. The weight in a voxel for measurements from source–detector pair  $sd$  is

$Wt(r_{sv}, r_{vd}) = Wt(r_{sv})Wt(r_{vd})$ , where

$$Wt(r_{sv}) = \left\{ \frac{\exp(-2k_r r_{sv})}{r_{sv}^2} + \frac{\exp(-2k_i r_{sv})}{r_{sv}^2} - 2 \frac{\exp[-k_i(r_{sv} + r_{I,v})]}{r_{sv} r_{I,v}} \cos[k_r(r_{sv} - r_{I,v})] \right\}^{0.5}$$

$$Wt(r_{vd}) = \left\{ \frac{\exp(-2k_r r_{vd})}{r_{vd}^2} + \frac{\exp(-2k_i r_{vd})}{r_{vd}^2} - 2 \frac{\exp[-k_i(r_{vd} + r_{I,d})]}{r_{vd} r_{I,d}} \cos[k_r(r_{vd} - r_{I,d})] \right\}^{0.5}. \quad (7)$$

Here  $r_{I,v}$  ( $r_{I,d}$ ) is the distance between the image source (image

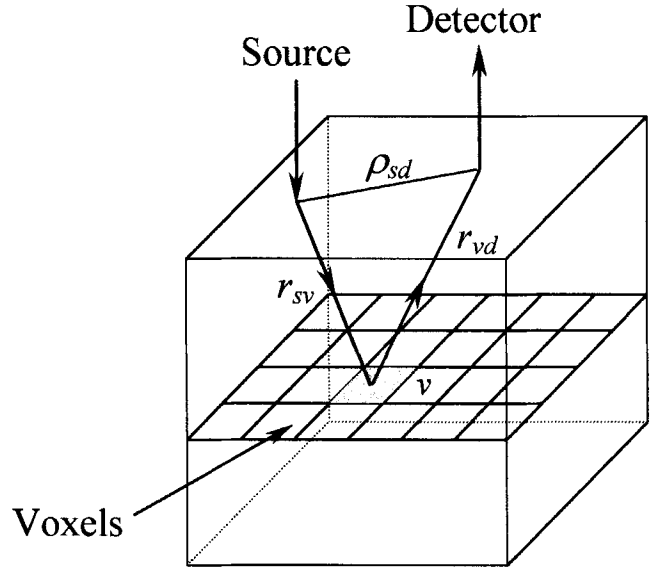


**Figure 4.** Geometrical configuration of a reconstructed planar slice. This figure shows only one source–detector pair. Measurements from all source–detector pairs are combined using weights to determine the optical properties  $\mu_a(r_v)$  and  $\mu_s(r_v)$  for each voxel in the slice.

voxel) and voxel (detector), required to satisfy the semi-infinite boundary condition. Values of the optical properties in a voxel located at  $r_v$  are calculated using the following equations:

$$\mu_a(r_v) = \frac{\sum_{sd} Wt(r_{sv}, r_{vd}) \mu_a^M(\rho_{sd})}{\sum_{sd} Wt(r_{sv}, r_{vd})}$$

and

$$\mu_s(r_v) = \frac{\sum_{sd} Wt(r_{sv}, r_{vd}) \mu_s^M(\rho_{sd})}{\sum_{sd} Wt(r_{sv}, r_{vd})}. \quad (8)$$

The sums are over all possible source–detector pairs on the pad. In practice, the voxels are 0.5 cm on a side and we compute these averages for all voxels in the planar slice.

Equations 7 and 8 enable us to create a qualitative image of absorption and scattering for a planar slice in the medium beneath the detector plane. Our choice of depth for the reconstructed slice may be dictated by *a priori* information about the depth of heterogeneity in the sample, or we can choose an intermediate depth set by the minimum source–detector separation on the surface. In general, although we are clearly sensitive to relatively deep structures ( $\sim 4$  cm below surface under realistic tissue conditions), we have found that reconstructions derived using our back-projection method vary slowly with respect to the depth variable. Nevertheless, we have found that the single-pad configuration gives useful two-dimensional images parallel to the plane of the pad.

## 5. MODEL STUDIES

In order to test the regional imager and to assess the utility of our back-projection reconstruction approach, we first test-

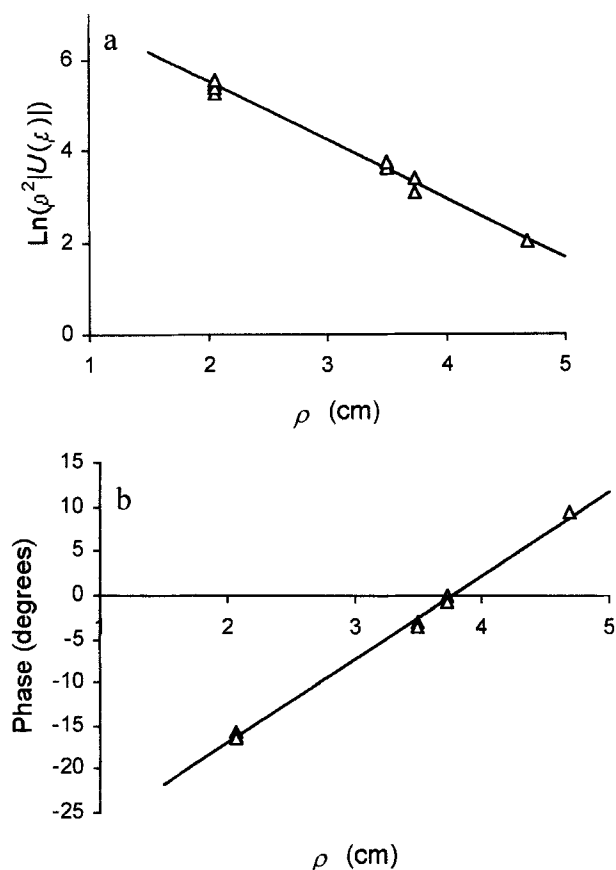


**Figure 5.** Average optical properties measured with the regional imager of a uniform intralipid sample with India ink. The triangles show measured data points from different sources for a single detector of the system. The solid lines show the best fit lines to the measured data. The slopes of the lines give the imaginary (a) and real (b) parts of  $k$ ; *i.e.*  $k_i = 1.28 \pm 0.05 \text{ cm}^{-1}$  and  $k_r = 0.166 \pm 0.003 \text{ rads cm}^{-1}$ . These give  $\mu_s = 5.1 \text{ cm}^{-1}$  and  $\mu_a = 0.11 \text{ cm}^{-1}$ .

ed the instrument on model systems. Our models consisted of a rectangular glass aquarium filled with an intralipid solution. The concentration of the intralipid in water was 0.5%. Black India ink was added to give an absorption coefficient of  $\sim 0.1 \text{ cm}^{-1}$ , similar to that expected for neonates. The dimensions of the aquarium are  $30 \text{ cm} \times 15 \text{ cm} \times 15 \text{ cm}$ . To incorporate the semi-infinite boundary condition, the optical pad was placed from the top of the aquarium against the liquid so that the ends of the optical fibers touched the liquid surface. The optical pad was centered with respect to the aquarium, with the long axis of the optical pad (9 cm) along the long axis (30 cm) of the aquarium. Various perturbing heterogeneities were submersed in the aquarium below the pad.

#### Average Optical Properties

We measured the average optical properties of the intralipid-ink solution using the method described in section 4. Figure 5 shows plots of  $\ln(\rho^2|U(\rho)|)$  and phase ( $\phi[\rho]$ ) versus the source-detector separation  $\rho$  for one of the detectors. The data was obtained using a modulation frequency of 100 MHz and a wavelength of 834 nm. The slopes of the lines give the imaginary (a) and real (b) components of  $k$ , respectively.

The data points are corrected for systematic variations in amplitude and phase between the different source fibers. These variations in amplitude and phase were determined by placing each source fiber in the same position with respect to a detector on a tissue model. The data points are also corrected for systematic phase variations of the detection circuits. Figure 5 shows data from only one of the detection channels; we make similar fits to data from the other detectors and then average the results of all four detection channels. This method of separately fitting the data from each detector eliminates errors resulting from systematic variations of amplitude and phase between the different detection channels. For all channels, measurements were rejected if the amplitude was less than the threshold where the response of the detection circuit departs significantly from being linear.

Our measurements of the average optical properties were consistently within 10–15% of one another, including measurements at different modulation frequencies and both wavelengths. For verification, we measured the absorption coefficient using a spectrophotometer of the India ink solution that we mixed with the intralipid. We also compared measurements from the regional imager to those from a second frequency domain instrument (infinite geometry) at the University of Pennsylvania (20,38). In order to assess any spurious effects associated with geometry, we also compared measurements taken on the same samples for an infinite geometry (we submersed a single source and detector into the middle of the aquarium and then measured the amplitude and phase for different source-detector separations). As an example, the optical properties derived from the data shown in Fig. 5 averaged with the results from the other three detection channels gives  $\mu_s = 4.97 \pm 0.36 \text{ cm}^{-1}$  and  $\mu_a = 0.115 \pm 0.01 \text{ cm}^{-1}$ . These agree reasonably well with the values of  $\mu_s = 5.0 \text{ cm}^{-1}$  and  $\mu_a = 0.095 \text{ cm}^{-1}$  derived from the known properties of the intralipid and the spectrophotometer measurements of the ink solution, as well as with the values derived from the infinite-medium geometry where  $\mu_s = 4.60 \pm 0.14 \text{ cm}^{-1}$  and  $\mu_a = 0.11 \pm 0.01 \text{ cm}^{-1}$ . All errors are standard deviations.

#### Image reconstruction in tissue phantoms

In all of our image reconstructions it was necessary to determine the initial amplitude and phase of the sources ( $S$  in Eq. 1). These source terms are determined from measurements of a reference tissue model with known optical properties. For the model studies presented here, this reference phantom consisted of the same intralipid solution without the submersed rod or test tubes.

Figure 6 shows two reconstructed slice images of a cylindrical rod placed inside the aquarium at two different locations near the optical pad using a modulation frequency of 100 MHz and a wavelength of 834 nm. The embedded object was a strongly absorbing black Delrin plastic rod, with a diameter of 1.3 cm. The axis of the cylindrical rod was oriented along the short axis of the pad at a depth of 2.5 cm from the pad. The transverse position and shape of the rod were found quite well. We obtained similar transverse images using a range of slice depths in the reconstruction; this is due, at least in part, to the emphasis placed by the weight

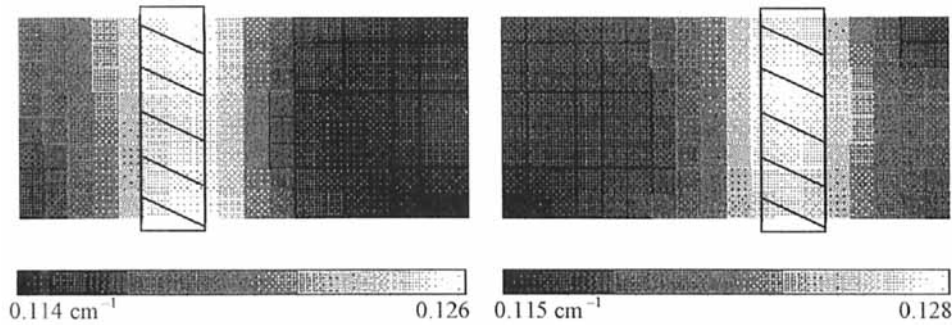


**Figure 6.** Reconstructed images of  $\mu_a$  for two different locations of an embedded absorber. The cross-hatched bar shows the actual position of the strongly (essentially infinitely) absorbing embedded rod. The size of the images is  $9 \times 4$  cm; the diameter of the rod is 1.3 cm. The rod was located 2.5 cm deep into the intralipid solution. The reconstructed images accurately show increased absorption at the locations of the embedded absorber.

function on measurements with shorter source–detector separations. While the back-projection method correctly predicted that the cylinder was more absorbing than the background medium, the magnitude of the absorption variation was incorrect. In general we find that the reconstructed optical properties of embedded heterogeneities tend to have values very close to those of the background medium. A more sophisticated reconstruction approach is clearly required to construct optical properties of embedded heterogeneities more accurately. We obtained similar results for measurements using a wavelength of 779 nm.

In a second model study, we used the wavelength and imaging capability to detect blood and to distinguish between oxygenated and deoxygenated blood. We used the same aquarium model described above. For this measurement, test tubes (with a diameter of 1.7 cm) were filled with either deoxygenated or oxygenated rabbit (whole) blood and were placed in the same location in the aquarium for both measurements. The test tubes contained an appropriate amount of intralipid, in addition to the blood, so that the scattering coefficient was approximately the same as for the intralipid solution in the aquarium. The test tubes were placed at a depth of 2.0 cm and oriented along the short axis of the optical pad. For each test tube, we made separate measurements using light with a wavelength of 779 and 834 nm; we then subtracted the image of  $\mu_a$  at 779 nm from the image of  $\mu_a$  at 834 nm on a voxel-by-voxel basis.

Figure 7 shows these differenced images for both blood with DeoxyHb (a) and blood with OxyHb (b). In Fig. 7a, the lightest region, which corresponds to a decrease in the absorption coefficient at 834 nm compared to at 779 nm, matches the position and orientation of the test tube of DeoxyHb blood. This correctly shows that the absorption coefficient of DeoxyHb blood is significantly larger at 779

nm than at 834 nm. In Fig. 7b, the darkest region, which corresponds to an increase in the absorption coefficient at 834 nm compared to at 779 nm, matches the position and orientation of the test tube of OxyHb blood. This correctly shows that the absorption coefficient of OxyHb blood is significantly larger at 834 nm than at 779 nm.

Although our measurements are qualitatively correct, the values of the absorption coefficients are not accurate. The reconstructed  $\mu_a$  for the test tubes of DeoxyHb (OxyHb) blood were  $0.026$  ( $0.029$ )  $\text{cm}^{-1}$  at 834 nm and  $0.034$  ( $0.015$ )  $\text{cm}^{-1}$  at 779 nm in excess of the average  $\mu_a$  ( $\sim 0.11$   $\text{cm}^{-1}$ ) of the intralipid-ink solution in the aquarium. (These are slightly larger than  $\mu_a$  determined for the black rod in Fig. 6 because the test tubes were located closer to the optical pad.) For the concentration of blood used, we estimated using the extinction coefficients from Zijlstra *et al.* (39) that  $\mu_a$  of the DeoxyHb and OxyHb blood samples was centered near  $0.5$   $\text{cm}^{-1}$  for our wavelengths. For both types of blood, we estimated that the difference in  $\mu_a$  at 834 and 779 nm is about  $0.2$   $\text{cm}^{-1}$  for our blood samples.

## 6. PRELIMINARY CLINICAL STUDY: HYDROCEPHALUS SHUNT

We have begun to conduct physiological studies on human volunteers. We report here one of these preliminary studies of a patient with hydrocephalus who was undergoing surgery to have a shunt replaced. Hydrocephalus is an abnormal increase in the amount of cerebrospinal fluid, which is a clear fluid, within the cranial cavity. We measured the patient immediately before surgery while the patient was anesthetized. The time required to measure a single image is about 2.5 min. The optical pad was placed on a shaved region of the patient's head above the top of the shunt (see Fig. 8). The

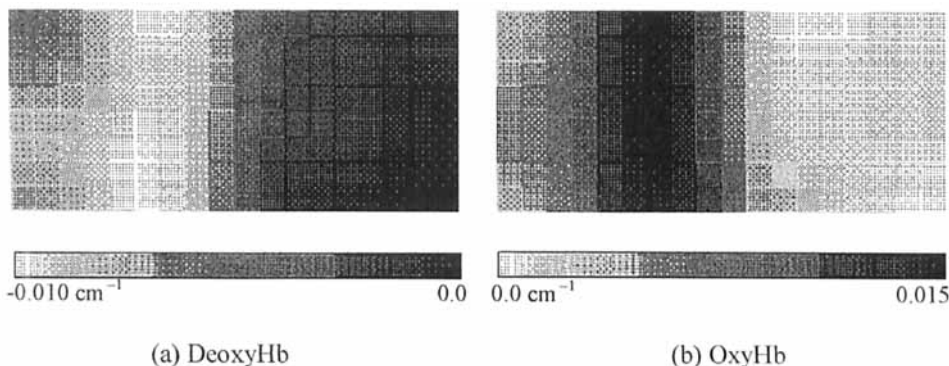
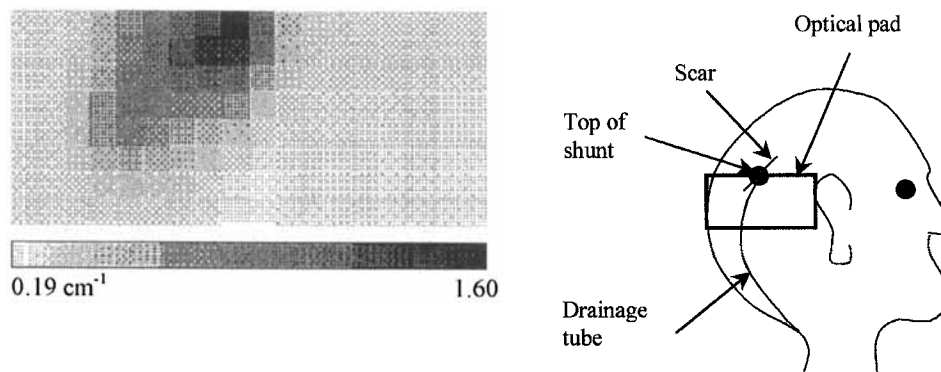


**Figure 7.** Differenced images of a test tube filled with (a) blood with DeoxyHb and (b) blood with OxyHb. These images show the difference in the reconstructed absorption coefficient  $\mu_a$  between that at 834 nm and that at 779 nm (*i.e.* 834–779 nm). The size of each image is  $9 \text{ cm} \times 4 \text{ cm}$ ; the test tube has a diameter of 1.7 cm and was located 2 cm below the pad.

**Figure 8.** Image of shunt. The image shows the reconstructed  $\mu_a$  of a region is  $9\text{ cm} \times 4\text{ cm}$  in dimension. The diagram of the head shows the orientation of the optical pad, which defines the region of the image, with respect to the head and the position of the shunt. The darkest region in the upper midsection of the image accurately matches the position of the top of the shunt; the extension of the dark region toward the lower left shows the drainage tube.



shunt is a plastic tube with a valve at one end (top). The valve is a hollow aluminum disk with a Teflon® cover. The valve diameter was  $\sim 1\text{ cm}$  and was located  $\sim 1.2\text{ cm}$  inside the surface of the skin. The plastic tube went through the brain (away from the skull and optical pad) to a ventricle. Another plastic tube, the drainage tube, went from the valve toward the neck, along the outer surface of the skull.

Figure 8 shows an image from this study, reconstructed at a depth of  $1.2\text{ cm}$ . The image was made using a modulation frequency of  $100\text{ MHz}$  and wavelength of  $834\text{ nm}$ . The image clearly shows the top (valve) of the shunt: the darkest region in the upper midsection of the image accurately matches the position of the shunt. The extension of the dark region toward the lower left shows the drainage tube. In order to obtain this image, we modified the optical pad slightly, so that the fibers were placed against the curved head by use of spring-actuated fiber connectors. A reference measurement of an intralipid-ink solution was used to determine the initial amplitude and phase of the sources (S in Eq. 1). These first *in vivo* measurements using the regional imager are clearly still preliminary but indicate the potential of the instrument.

## 7. CONCLUSION

We described a new instrument that we have developed for low-resolution functional imaging of the brain with diffusing near-infrared light. The unit combines spectroscopic and imaging modalities enabling the clinician to discriminate bulk tissue behavior from the contributions of localized regions ( $\sim 1\text{ cm}^3$  in size) of tissue. We have tested the regional imager on some models and have started studies of pediatric patients at the Children's Hospital of Philadelphia.

**Acknowledgements**—This work is supported by contract N44-NS-5-2317 from NINDS. We thank David Boas, Britton Chance, Phil Farnum, Dean Kurth, Shoko Nioka and Maureen O'Leary for many useful conversations. We thank Dean Kurth and Hilary Klein for coordinating and assisting with clinical studies. We thank Lee Sutton for assisting with clinical studies. A.G.Y. acknowledges partial support from the NSF DMR96-23441.

## REFERENCES

- Yodh, A. and B. Chance (1995) Spectroscopy and imaging with diffusing light. *Physics Today* **48**, 34–40.
- Chance, B. and R. R. Alfano (eds.) (1995) In *Proceedings of Optical Tomography, Photon Migration, and Spectroscopy of Tissue and Model Media: Theory, Human Studies, and Instrumentation*, Vols. I, II. SPIE **2389**.
- Gratton, E., W. Mantulin, M. J. van de Ven, J. Fishkin, M. Maris and B. Chance (1990) *Proceedings of the Third International Conference: Peace through Mind/Brain Science*, pp. 183–189. August 5–10, Hamamatsu, Japan.
- O'Leary, M. A., D. A. Boas, B. Chance and A. G. Yodh (1992) Refraction of diffuse photon density waves. *Phys. Rev. Lett.* **69**, 2658–2661.
- Boas, D. A., M. A. O'Leary, B. Chance and A. G. Yodh (1993) Scattering and wavelength transduction of diffuse photon density waves. *Phys. Rev. E* **47**, R2999–3003.
- Fishkin, J. and E. Gratton (1993) Propagation of photon density waves in strongly scattering media containing an absorbing "semi-infinite" plane bounded by a straight edge. *J. Opt. Soc. Am. A* **10**, 127–140.
- Tromberg, B., L. O. Svaasand, T. Tsay and R. C. Haskell (1993) Properties of photon density waves in multiply scattering media. *Appl. Opt.* **32**, 607–616.
- Sevick, E. M., J. Lakowicz, H. Szmecinski, K. Nowaczyk and M. L. Johnson (1992) Frequency domain imaging of absorbers obscured by scattering. *J. Photochem. Photobiol. B* **16**, 169–185.
- Schmitt, J. M., A. Knuttel and J. R. Knudsen (1992) Interference of diffusive light waves. *J. Opt. Soc. Am. A* **9**, 1832.
- Patterson, M. S., B. Chance and B. C. Wilson (1989) Time-resolved reflectance and transmittance for the noninvasive measurement of tissue optical properties. *Appl. Opt.* **28**, 2331–2336.
- Delpy, D. T., M. Cope, P. van de Zee, S. Arridge, S. Wray and J. Wyatt (1988) Estimation of optical pathlength through tissue from direct time of flight measurement. *Phys. Med. Biol.* **33**, 1433–1442.
- Jacques, S. L. (1989) Time resolved propagation of ultrashort laser pulses within turbid tissues. *Appl. Opt.* **28**, 2223–2229.
- Benaron, D. A., D. C. Ho, S. Spilman, J. P. van Houten and D. K. Stevenson (1994) Tomographic time-of-flight optical imaging device. *Adv. Exp. Med. Biol.* **361**, 207–214.
- Ishii, M., J. Leigh and J. Schotland (1995) Photon diffusion imaging in model and biological systems. In *Optical Tomography, Photon Migration and Spectroscopy of Tissue and Model Media: Theory, Human Studies and Instrumentation*, p. 312. SPIE Optical Engineering Press, Bellingham, WA.
- Zhu, W., Y. Wang, J. Chang, H. L. Graber and R. L. Barbour (1995) A total least squares approach for the solution of the perturbation equation. In *Optical Tomography, Photon Migration and Spectroscopy of Tissue and Model Media: Theory, Human Studies and Instrumentation*, pp. 420–430. SPIE Optical Engineering Press, Bellingham, WA.
- Chang, J., H. Graber and R. L. Barbour (1995) Image reconstruction of dense scattering media from CW sources using constrained CGD and a matrix scaling technique. In *Optical Tomography, Photon Migration and Spectroscopy of Tissue and Model Media: Theory, Human Studies and Instrumentation*, pp. 682–691. SPIE Optical Engineering Press, Bellingham, WA.
- Arridge, S. R. (1993) In *Medical Optical Tomography: Functional Imaging and Monitoring*, Vol. IS11 (Edited by G. Muller et al.), pp. 31–64. SPIE Optical Engineering Press, Bellingham, WA.
- O'Leary, M. A., D. A. Boas, B. Chance and A. G. Yodh (1995)

- Experimental images of heterogenous turbid media by frequency-domain diffusing-photon tomography. *Opt. Lett.* **20**, 426–428.
19. Pogue, B. M., M. S. Patterson, H. Jiang and K. D. Paulson (1995) Initial assessment of a simple system for frequency domain diffuse optical tomography. *Phys. Med. Biol.* **40**, 1709–1729.
  20. Li, X. D., T. Durduran, A. G. Yodh, B. Chance and D. N. Pattanayak (1997) Diffraction tomography for biomedical imaging with diffuse photon density waves. *Opt. Lett.* **22**, 573–575.
  21. Franceschini, M. A., K. T. Moesta, S. Fantini, G. Gaida, E. Gratton, H. Jess, M. Seeber, P. M. Schlag and M. Kashke (1997) Frequency-domain techniques enhance optical mammography: initial clinical results. *Proc. Natl. Acad. Sci. USA* **94**, 6468–6473.
  22. Fantini, S., M. A. Franceschini, G. Gaida, E. Gratton, H. Jess, W. M. Mantulin, K. T. Moesta, P. M. Schlag and M. Kashke (1996) Frequency-domain optical mammography: edge effect corrections. *Med. Phys.* **23**, 1–9.
  23. van Houten, J., D. Benaron, S. Spilman and D. Stevenson (1996) Imaging brain injury using time-resolved near-infrared light scanning. *Pediatric Res.* **39**, 470.
  24. Boas, D. A., M. A. O'Leary, B. Chance and A. G. Yodh (1997) Detection and characterization of optical inhomogeneities with diffuse photon density wave: a signal-to-noise analysis. *Appl. Opt.* **36**, 75–92.
  25. Gopinath, S. P., C. S. Robertson, R. Grossman and B. Chance (1993) Near-infrared spectroscopic localization of intracranial hematomas. *J. Neurosurg.* **79**, 43–47.
  26. Brazy, J. (1991) Cerebral oxygen monitoring with near-infrared spectroscopy: clinical application to neonates. *J. Clin. Monit.* **7**, 325–324.
  27. Delpy, D., M. Cope, E. B. Cady, J. S. Wyatt, P. A. Hamilton, P. L. Hope, S. Wray and E. O. Reynold (1987) Cerebral monitoring in newborn infants by magnetic resonance and near-infrared spectroscopy. *Scand. J. Clin. Lab. Invest.* **47**(Suppl. 188), 9–17.
  28. Smith, D. S., W. Levy, M. Maris and B. Chance (1990) Reperfusion and hyperoxia in brain after circulatory arrest in humans. *Anesthesiology* **73**, 12–19.
  29. Fantini, S., M. A. Franceschini, J. B. Fishkin, B. Barbieri and E. Gratton (1995) Quantitative determination of the absorption spectra of chromophores in strongly scattering media: a light-emitting-diode-based technique. *Appl. Opt.* **33**, 5204–5213.
  30. Fishkin, J. B., O. Coquoz, E. R. Anderson, M. Brenner and B. J. Tromberg (1997) Frequency-domain photon migration measurements of normal and malignant tissue optical properties in a human subject. *Appl. Opt.* **36**, 10–20.
  31. Nichols, M. G., E. L. Hull and T. H. Foster (1997) Design and testing of a white-light, steady-state diffuse reflectance spectrometer for determination of optical properties of highly scattering systems. *Appl. Opt.* **36**, 93–104.
  32. Jobsis, F. F. (1977) Noninvasive infrared monitoring of cerebral and myocardial oxygen sufficiency and circulatory parameters. *Science* **198**, 1264–1267.
  33. Wilson, B. D., T. J. Farrell and M. S. Patterson (1990) An optical fiber-based diffuse reflectance spectrometer for non-invasive investigation of photodynamic sensitizers in-vivo. In *Future Direction and Applications in Photodynamic Therapy*, Vol. IS6 (Edited by C. J. Gomer), pp. 219–232. SPIE Institute Series, Bellingham, WA.
  34. Madsen, S. J., E. R. Anderson, R. C. Haskell and B. J. Tromberg (1994) Portable high-bandwidth frequency-domain photon migration instrument for tissue spectroscopy. *Opt. Lett.* **19**, 1934–1936.
  35. Cope, M. and D. T. Delpy (1996) A system for the long-term measurement of cerebral blood and tissue oxygenation in newborn infants by near-infrared transillumination. *Med. Biol. Eng. Comput.* **26**, 289–294.
  36. Haskell, R. C., L. O. Svaasand, T. Tsay, T. Feng, M. S. McAdams and B. J. Tromberg (1994) Boundary conditions for the diffusion equation in radiative transfer. *J. Opt. Soc. Am. A* **11**, 2727–2741.
  37. Kak, A. and M. Slaney (1988) *Principles of Computerized Tomographic Imaging*. IEEE Press, New York.
  38. Yang, Y., H. Liu, X. Li and B. Chance (1997) Low-cost frequency-domain photon migration instrument for tissue spectroscopy, oximetry, and imaging. *Opt. Eng.* **36**, 1562–1569.
  39. Zijlstra, W. G., A. Buursma and W. P. Meeuwse-van der Roest (1991) Absorption spectra of human fetal and adult oxyhemoglobin, de-oxyhemoglobin, carboxyhemoglobin, and methemoglobin. *Clin. Chem.* **37**, 1633–1638.